Full Length Article

Microstructure and mechanical behavior of similar butt-joints of ZK60 and ZK60–1.5RE magnesium alloys produced by linear friction stir welding

Erenilton Pereira da Silva[a,*], Ricardo Henrique Buzolin[c,d], Ulises Alfaro[e], Guillermo Requena[e,f], Haroldo Calvalcanti Pinto[b]

[a] *Institute of Engineering, Science and Technology (IECT), Federal University of Vales do Jequitinhonha e Mucuri (UFVJM), Janaúba, MG, Brazil*
[b] *Department of Materials Engineering, São Carlos School of Engineering (EESC), University of São Paulo (USP), São Carlos-SP CEP 13563-120, Brazil*
[c] *Christian Doppler Laboratory for Design of High-Performance Alloys by Thermomechanical Processing, Kopernikusgasse 24, Graz 8010, Austria*
[d] *Institute of Materials Science, Joining and Forming at Graz University of Technology opernikusgasse 24/I, Graz 8010, Austria*
[e] *German Aerospace Center (DLR) Institute of Materials Research, Linder Höhe, Cologne 51147, Germany*
[f] *RWTH Aachen University, Metallic Structures and Materials Systems for Aerospace Engineering, D-52062 Aachen, Germany.*

Abstract

The microstructure and mechanical properties of butt-joints produced by linear friction stir welding of similar plates of as-cast ZK60 and modified ZK60 with 1.5 wt.% RE (ZK60–1.5RE) are investigated. The thermomechanical affected zone is investigated in both advancing and retrieving sides, and the microstructure is compared to the base metal and the stirred zone. Electron backscattered diffraction measurements provide the average microstructural features of the transformed microstructure. The mechanical properties are assessed using hardness, tensile testing, and surface residual stress measured using X-ray diffraction. Higher torque and heat input are obtained for the ZK60–1.5RE compared to the ZK60. The thermomechanical affected zone is notably larger for the ZK60 compared to the ZK60–1.5RE. A gradient microstructure is formed in thermomechanical affected zones where deformed grains are progressively more recrystallised towards the stirred zone. There is no visible interface between the thermomechanical affected zone and the stirred zone. A fine and partially recrystallised microstructure is formed in the stirred zone. The retrieving side of the ZK60–1.5RE has a slightly more refined microstructure compared to the other investigated zones. Anisotropy measured with increment in the maximum intensity of the (0001) increases towards to stirred zone. The formed microstructure is correlated with the role of twinning, recovery, static, and dynamic recrystallisation that can occur during friction stir welding. Twinning and grains with large misorientation spread are more pronounced in the thermomechanical affected zone and regions towards the base metal. Sharp low angle grain boundaries are observed towards the stirred zone. From refined recrystallised grains decorating the grain in the thermomechanical affected zone, a mosaic-like of low and high angle grain boundaries are observed in the stirred zone. The joints have comparable surface residual stresses. The friction stir welding improved the ductility and strength of the as-cast ZK60–1.5RE alloy since the tensile samples fractured in the BM.

1. Introduction

Due to the remarkable specific properties and being one of the most lightweight metals, magnesium alloys have been intensively investigated to broaden its applications [1,2]. The thermomechanical treatment of ZK60 alloy shows that the

* Corresponding author.
 E-mail address: erenilton.silva@ufvjm.edu.br (E.P. da Silva).

restoration mechanisms depend on the deformation conditions [3,4]. Dynamic recrystallisation (DRX) associated with deformation twinning, basal slip, and $(a + c)$ dislocation glide occurs below 200 °C [4]. Continuous dynamic recrystallisation (CDRX) occurs at intermediate temperatures (between 200 °C to 250 °C) due to extensive cross-slip [3,4]. For temperatures higher than 250 °C, DRX occurred via bulging of grain boundaries and sub-grain growth, i.e., discontinuous dynamic recrystallisation (DDRX) [4–6]. Complementary, Wu et al. [7] concluded that ZK60 forms twins with high dislocation density divide the parent grains, followed by dislocation arrays and low-angle grain boundaries within the twins to DDRX at higher strains. The addition of Ce to the ZK60 leads to enhancement of DRX by particle stimulated nucleation at Mg-Zn-Ce particles [8–10]. Moreover, the Ce addition weakened the basal fibre texture.

Friction stir welding (FSW) has shown to be a promising technique for similar and dissimilar joints of magnesium alloys [11–13]. FSW is regarded as a solid-state joining process, and due to the hot plastic deformation, a fine-grained structure is produced [14–17]. The impact of the corrosion resistance of joints of magnesium alloys produced by FSW is not straightforward. Dispersion of second phases (mainly $Mg_{17}Al_{12}$ in AZ alloys) can decrease the corrosion resistance [18,19]. However, the formation of a recrystallised and homogeneous α-matrix [20,21], and formation of specific texture [22] can enhance the corrosion resistance of the FSW joints in comparison to the base metal (BM). The creep behaviour of joints of AE42 produced via FSW improved compared to the as-cast BM due to the refinement of the microstructure and dispersion of fine intermetallic compounds pinning the grain boundaries [23]. The fatigue properties were investigated [24,25] and are strongly correlated to microstructural features (grain size, twinning fraction, recrystallisation grade), and the micro and macro texture obtained at the nugget as well as in the thermomechanical affected zone (TMAZ) [26]. Therefore several attempts on controlling the evolved texture have been investigated [26,27], and the formation of a weak texture is beneficial for joint performance. Larger but recrystallised grains seem to increase the elongation of the FSWed joints [28]. However, understanding the correlation between processing parameters and microstructure formation requires further investigation.

Liu et al. [29] investigated in detail the evolution of the microstructure of an FSW joint of AZ31 magnesium alloy for a wide range of welding conditions and due to the formation of a strong $\{0001\}<u$ w t $v>$ B-fibre texture, the controlling of the grain structure is limited. Complex restorations mechanism plays a role in the microstructure formation in FSW [30], and they are directly correlated to the thermomechanical behaviour of the material [4]. Despite the intensive research on the characterisation of the produced joints and its properties [31], there is the need to understand better the complex interaction of the deformation mechanisms and the microstructure modification of ZK60 alloys during FSW. Thus, it can provide the necessary insights to tune the microstructure and consequently, the mechanical properties of

the FSW joints. among high strength magnesium alloys, the ZK60 (Mg-6.0Zn-0.6Zr (wt.%)) alloy offers a good compromise between high strength and ductility requirements and low cost in production. Investigations on the effect of RE addition on Mg alloys are extensive and Mg alloys with rare earth (RE) addition show potential for achieving improved strength and creep resistance compared with the AZ system [32–34]. Besides, enhanced room temperature tensile strength and ductility at room temperature [35,36], are reported. Magnesium alloys based on RE additions exhibited a fully recrystallised microstructure with weak texture after friction stir processing (a derived technique from FSW) [37], a notable improvement in texture microstructure control in comparison to other magnesium alloys.

This work aims to: a) establish microstructure modification mechanisms during FSW of ZK60; b) find the influence of Ce on the microstructure formation during FSW of a ZK60 modified with 1.5 wt.% mischmetal based on Ce (hereon named ZK60–1.5RE). Despite generally being wrought alloys, the modified ZK60 alloys are investigated in the as-cast state to provide a non-deformed BM as the baseline for comparing the microstructural changes during FSW. The microstructure of the two similar joints is systematically investigated and correlated to the room temperature mechanical properties.

2. Experimental procedures

Plates of as-cast ZK60 and ZK60–1.5RE alloys were produced according to the processing route described in [9,38,39], and similar joints were produced using linear friction stir welding (FSW).

2.1. Linear friction stir welding (FSW)

An RM1 FSW machine was used to perform the linear FSW. The welded plates had 5.4 mm in thickness and 200 mm in length. AISI H13 steel tool with a 3° concave shoulder of diameter and an insertable pin with a conical base of 5 and 5 mm high were used. The plates were welded using a normal force of 15 kN, a rotation speed of 1200 rpm, and a 400 mm/min rotation speed with a tilt angle of 3° The heat input was calculated according to Eq. 1.

$$H = \frac{2\pi\omega T}{v} \tag{1}$$

Where ω is the rotation speed, T is the torque withstood by the tool, and v is the advancing velocity during FSW.

2.2. Microstructure characterisation

Samples were extracted from the joint in the cross-section and metallographically prepared using grinding followed by oxide polishing suspension (OPS) final polishing for microstructural investigation. An FEI Inspect FL50 scanning electron microscope (SEM) was used for acquiring secondary electrons (SE) micrographs while a Zeiss Ultra 55 was used for performing electron backscattered diffraction (EBSD) measurements.

2.3. Electron backscattered diffraction analysis (EBSD)

The software OIM Analysis v.8 was used to perform the EBSD data treatment. A misorientation angle of 15° defined a grain boundary and the minimum grain size considered was 1 μm in diameter. The grains were standardised to their confidence index, and a minimum confidence index of 0.2 was used for re-indexation to the neighbour grains. Low angle grain boundaries are defined with a misorientation angle between 2° and 15° while high angle grain boundaries are considered for a misorientation angle larger than 15° The tensile twins $\{10\bar{1}2\}\langle1\bar{2}10\rangle$ are excluded from the high angle grain boundaries for calculating the grains. The kernel average misorientation (KAM) was calculated to the second neighbour. Grains with misorientation spread lower than 2° are considered recrystallised, and the recrystallisation grade is evaluated using grain orientation spread. Geometric necessary dislocations (GND) density was calculated using the $\{0001\}\langle11\bar{2}0\rangle$, $\{1\bar{1}00\}\langle11\bar{2}0\rangle$, $\{1\bar{1}01\}\langle11\bar{2}0\rangle$, $\{10\bar{1}1\}\langle11\bar{2}3\rangle$ and $\{11\bar{2}2\}\langle11\bar{2}3\rangle$ slip system, considering the first nearest neighbour for a Burgers vector magnitude of 0.32 nm [40].

2.4. Mechanical properties

Microhardness maps of the cross-sections of the joints were performed for a polished surface using a load of 0.3 Kg in an MMT-X7 – CLEMEX hardness tester. A matrix of 17 lines and 69 columns with an interspace of 0.3 mm were used.

Tensile specimens with a gauge of 12 mm length, 6 mm width and 5 mm thickness [38] were extracted from the cross-sections of the produced joints. The tensile testing was performed according to the ASTM E8M deformed at a deformation speed of 0.074 mm/min coupled with image correlation using a D720 Nikon camera acquired during the tensile tests with an acquisition rate of 0.1 Hz and evaluated using the software Aramis®.

Surface residual stress measurements were performed using a Panalytical MRD-XL diffractometer with a Co X-Ray source and the method of $sin^2(\psi)$ [47]. Seven ψ angles between 0 and 76° for the Mg diffraction peaks of $(20\bar{2}1)$, $(11\bar{2}2)$ and $(10\bar{1}3)$ using a beam size of 2 mm per 2 mm with wobbling of 10 mm along the weld direction

3. Results

3.1. Welding parameters

The measured torque and heat input of the produced joints are shown in Fig. 1(a and b, respectively). Lower torque and heat input is achieved for the ZK60 alloy weld with lower variations in those parameters that are observed for the ZK60–1.5RE. The addition of RE to a ZK60 alloy led to slightly higher steady flow stresses for a given temperature and strain rate [41], mainly attributed to the hard and thermal stable RE containing intermetallic compounds. Thus, ~20% higher torques are necessary to weld the ZK60–1.5RE compared

to the ZK60. Since the advancing speed, and the rotation speed is the same for both joints, the heat input is also ~20% higher for ZK60–1.5RE than ZK60 joint due to higher torque for the ZK60–1.5RE (Eq. (1)). The maximum temperature achieved during FSW does not exceed the material melting point, which is 635 °C for the ZK60 alloy [42].

3.2. Microstructure characterisation

The cross-section light optical micrographs of the welded plates are shown in Fig. 2 for the ZK60 (Fig. 2a) and ZK60–1.5RE (Fig. 2b). The stirred zone (SZ) beneath the shoulder is extended for the ZK60 compared to the ZK60–1.5RE. Moreover, a visible thermomechanical affected zone (TMAZ) is observed for the ZK60, while its presence is not evident in the optical micrograph.

Fig. 3 shows the secondary electrons (SE-SEM) micrographs of the base metal (BM) (Fig. 3(a,e)), the TMAZ of the retreating side (RS) (Fig. 3(b,f)), the SZ (Fig. 3(c,g)) as well as the TMAZ of the advancing side (AS) (Fig. 3(d,h)). Arora et al. [42] estimated strains achieved during FSW in the range of −10 to 5, and strain rates from −9 s^{-1} to 9 s^{-1}. Higher strain rates above 900 s^{-1} were predicted for a dissimilar FSW joint [43]. Also, notable larger strains above 200 were predicted during FSW by Jain et al. [44]. A maximum strain rate of ~35 s^{-1} was estimated for an AZ31 during FSW [45]. Therefore, high strains and strain rates are expected to be achieved in the investigated joints. Silva et al. [38] investigated the investigated as-cast alloys reported in this work in more detail. The intermetallic compounds formed in the as-cast BM of ZK60 are the Mg_7Zn_3 (5.8 vol.%) and the Zn_2Zr (1.0 vol.%), while Mg_7Zn_3 (3.0 vol.%), $MgZn_2Ce$ (2.7 vol.%) and Zn_2Zr (1.0 vol.%) are formed in the as-cast BM of ZK60–1.5RE.

The plastic deformation at TMAZ leads to a partial disruption of the semi-continuous network of intermetallic compounds formed along the grain boundaries of the nearly-globular dendritic as-cast microstructure. A gradient of partially dissolved and partially fragmented intermetallic compounds is observed in the TMAZ in both AS and RS sides. Despite comparable volume fraction of intermetallic compounds at the BM, the $MgZn_2Ce$ are shown higher thermal stability. Thus, at the deformation temperatures achieved during the FSW, they can act as reinforcement at the matrix in the ZK60–1.5RE. Moreover, the high temperature and high strain rates partially dissolve the Mg_7Zn_3 at the SZ and are notable in Fig. 3c for the ZK60. The remaining intermetallic compounds are fragmented due to the notably large plastic deformations achieved in the SZ. The intermetallic particles are dispersed in the α-matrix in the SZ of both alloys (Fig. 3(c,h)), and aligned in "lines" due to the flow of material during FSW.

The typical microstructure of the joints produced by FSW is illustrated in the EBSD analysis shown in Fig. 4 for the ZK60–1.5RE. A large region where deformed grains are progressively recrystallised is observed in Fig. 4a. There is no sharp transition between the TMAZ and the SZ. Grains with
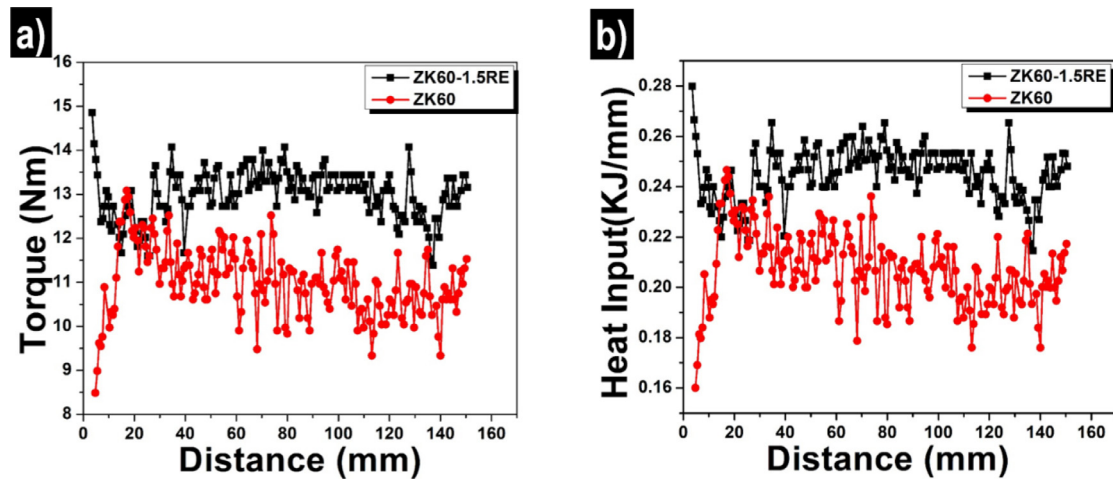
Fig. 1. Welding parameters of the investigated joints produced by FSW: a) torque; b) heat input.
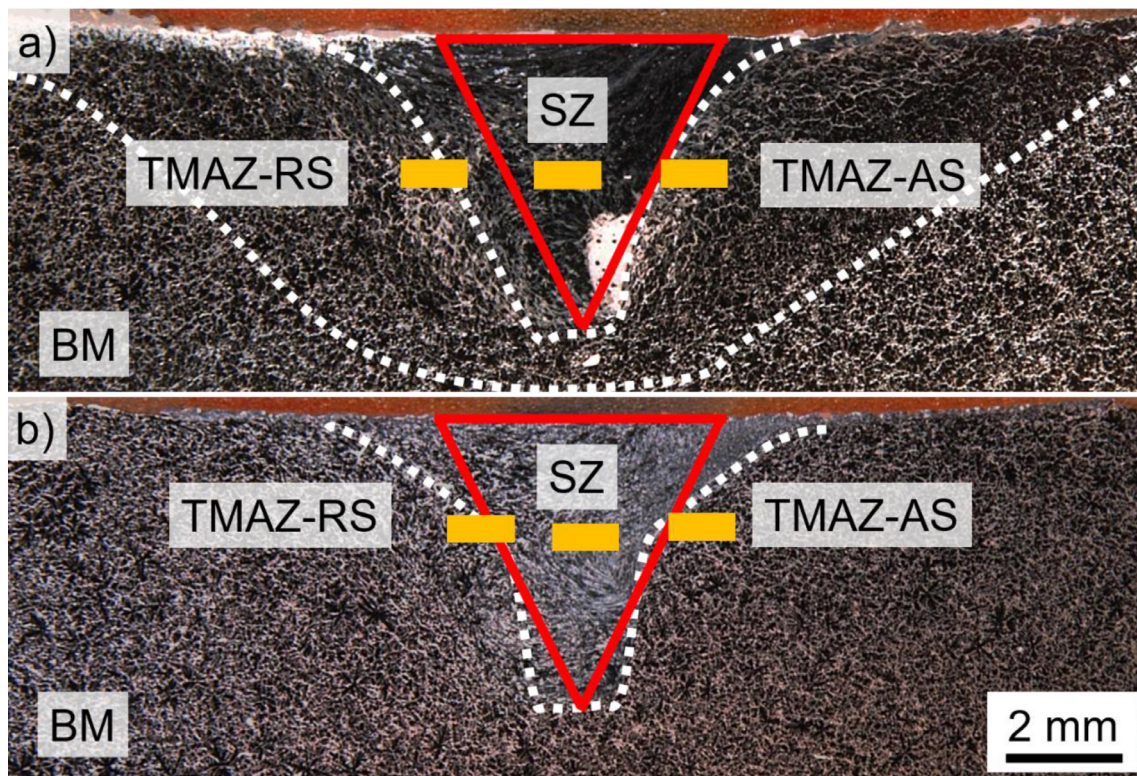

Fig. 2. Light optical micrographs of the cross-section of the produced joints: a) ZK60 alloy; b) ZK60–1.5RE alloy. The red triangle indicates the shape of the pin of the tool, the stirred zone and the thermomechanical affected zones are shown, and the retrieving and advancing sides. The yellow rectangles indicate the positions of the EBSD measurements.

misorientation spread lower than 2° are shown in Fig. 4d, while the grains with larger misorientation are shown in Fig. 4c. The misorientation spread of 2° is set here at the threshold for a recrystallised grain. The recrystallised grains are decorating the prior grain boundaries at locations in the TMAZ closer to the BM as shown in Fig. 4d indicated by the red circle. In contrast, a matrix with relatively randomly distributed recrystallised and deformed grains are observed towards the SZ. Therefore, the TMAZ of the investigate joints

consists mainly of a microstructural gradient from a coarse and deformed as-cast microstructure near the BM towards a refined and partially recrystallised microstructure at the SZ. The microstructure gradient observed for the ZK60–1.5RE-tixo is notably less pronounced for the same measurement area for the ZK60 due to the notably larger TMAZ for the ZK60, Fig. 2.

Fig. 5 shows the representative EBSD analysis of the different joint regions produced by FSW for the ZK60 alloy.
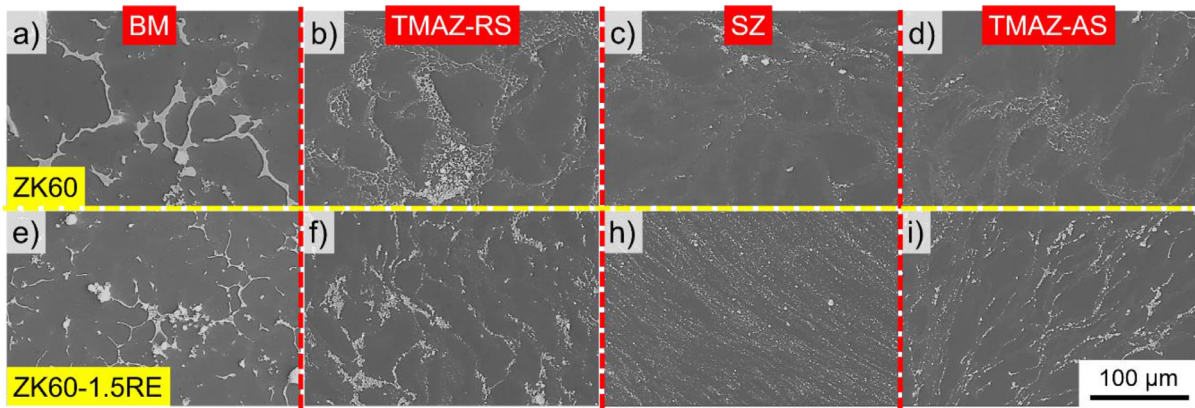
Fig. 3. Secondary electron (SEM-SE) micrographs of the cross-section of the investigated regions of the joint: a,e) base materials; b,f) thermomechanical affected zone at the retrieving side; c,g) stirred zone; d,h) thermomechanical affected zone at the advancing side. The micrographs correspond to the: a-d) ZK60 alloy; e-h) ZK60–1.5RE.
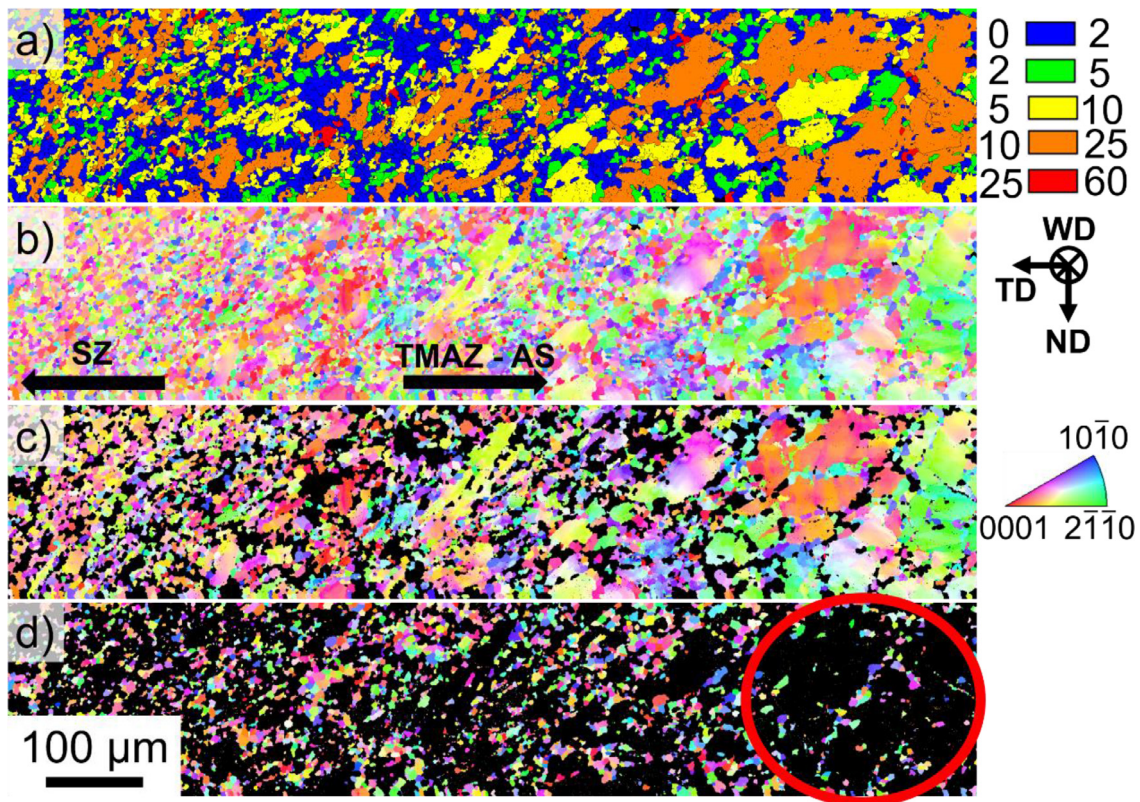

Fig. 4. Electron backscattered electrons diffraction of the thermomechanical affected zone of the advancing side for the cross-section of the joint of the ZK60–1.5RE alloy: (a) grain orientation spread map; (b) inverse pole figure map; (c) inverse pole figure map of the deformed fraction; (d) inverse pole figure map of the recrystallised fraction. The welding direction is perpendicular to the plane of the image, and the normal direction is indicated by ND and the transversal direction by TD. The base material is located towards the right and the stirred zone towards the left. The red circle indicates a region with recrystallised grains along prior grain boundaries.

For the investigated joints, an area at the centre of the investigated zone is exhibited. A notably refined microstructure is observed at the SZ. The flow lines of material can be inferred in the SZ by the oriented regions with aligned GBs, as indicated in Fig. 5k by the yellow lines. The presence of tensile twins $\{10\bar{1}2\}\langle1\bar{2}10\rangle$ is notable in the deformed grains in the TMAZ in both RS and AS (Fig. 5(j and l, respec-

tively)). A fully recrystallised region is not obtained in any of the investigated areas. In Fig. 5(g–i), the KAM maps show that in the TMAZ, deformed grains with a denser network of boundaries with larger KAM values are observed. However, the grains shown as recrystallised due to misorientation spread lower than 2° also show KAM values higher than zero in both TMAZ and SZ.
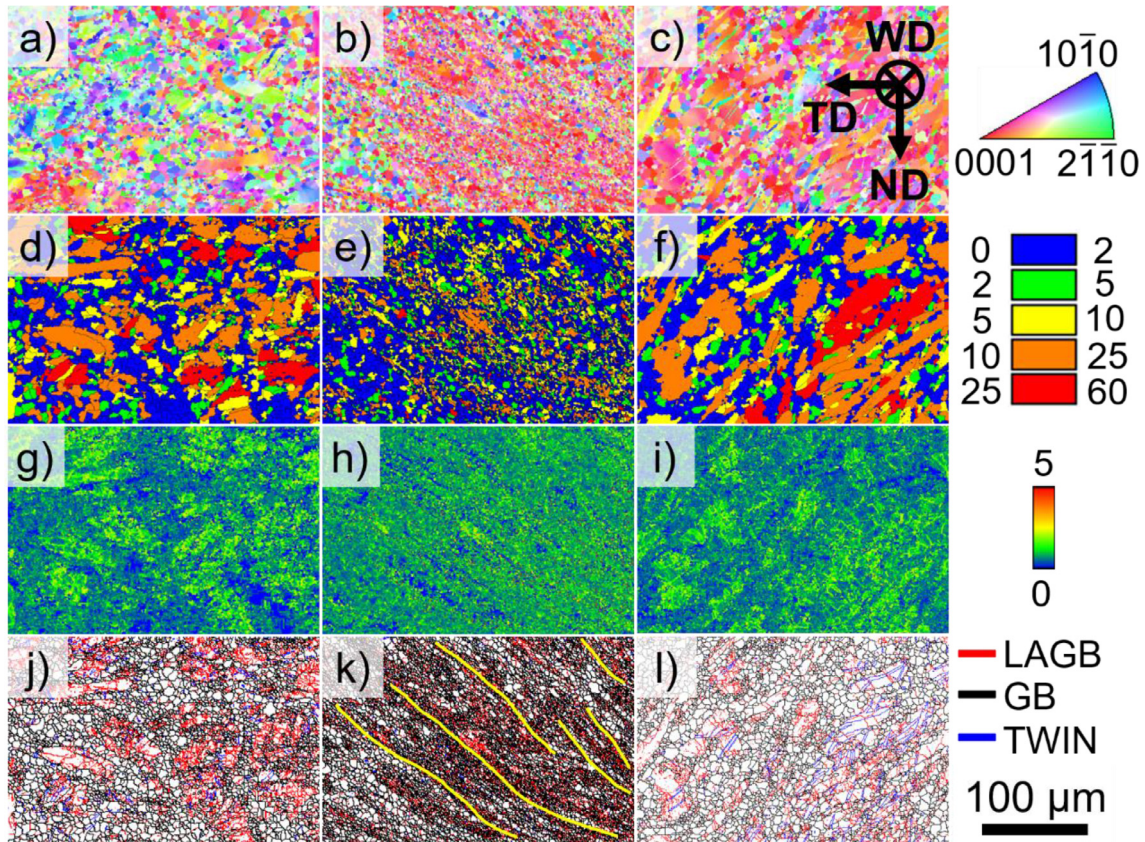
Fig. 5. Representative electron backscattered diffraction analysis of the joint of the ZK60 alloy for the cross-section of the three distinct regions: (a,d,g,j) retrieving side of the thermomechanical affected zone; (b,e,h,k) stirred zone; (c,f,i,l) advancing side of the thermomechanical affected zone. a-c: inverse pole figure maps; D-f: grain orientation spread maps; (g–i) kernel average misorientation maps; (j–l) boundary maps.

Fig. 6 shows the typical microstructure of the joint of ZK60–1.5RE produced by FSW: Similarly to the join of ZK60, a partially recrystallised microstructure is observed in the TMAZ in the AS (Fig. 6f) and RS (Fig. 6d) as well as in the SZ (Fig. 6e). For the investigated region, a fine microstructure is achieved in the RS (Fig. 6j) of the TMAZ compared to the AS (Fig. 6l). In both regions, recrystallised grains with KAM values close to zero as observed (Fig. 6g and i), while a nearly homogeneous matrix with non-zero KAM values is observed in the SZ (Fig. 6h). The presence of deformed grains with twins and large misorientation is observed at the AS of the TMAZ (Fig. 6(c,f,i,l)).

The mean geometric necessary dislocation (GND) density, grain size, and the maximum intensity of the pole figure for the (0001) are plotted in Fig. 7(a, b and c, respectively) for the investigated regions of the produced joints and are separated also for the deformed fraction and recrystallised fraction. The refinement of the microstructure at the SZ is notable. From an average grain size of ~250 μm for the ZK60 and ~150 μm for the ZK60–1.5RE, a mean recrystallised grain size of ~3.3 μm and ~4.3 μm are observed for the ZK60 and ZK60–1.5RE, respectively.

The higher heat input and the lower extent of the thermomechanical affected zone can be understood as larger dissipation at the SZ. Higher temperatures and/or longer durations of the peak temperature are expected for the ZK60–1.5RE in

comparison to the ZK60. Thus, a higher velocity of the high angle grain boundaries during dynamic and static recrystallisation, a higher nucleation rate during static recrystallisation, and a higher extent of dynamic recovery during deformation in the ZK60–1.5RE are attributed as the main reasons for the slightly larger recrystallised grain size observed ZK60–1.5RE alloy. The larger differences between recrystallised and deformed grain sizes are observed at the TMAZ in the AS. Moreover, the recrystallised grain size measured at the TMAZ is comparable to the grain size measured at the SZ. Comparable values of GNDs are observed in the stirred zone for both joints. The values of GNDs are the highest for the ZK60–1.5RE in the AS and slightly higher than those in comparison to the same region for the ZK60. The increase in the maximum intensity of the pole figure for the basal plane (0001) seems to increase from the base metal towards the stirred zone. The formation of an anisotropic material at the stirred zone can be explained by the intensive plastic deformation and preferential lattice rotation due to the preferential shear forces during FSW. However, the results are contrasting with the finding of Jamili et al. [37], where the texture was reduced after FSP. There are two main reasons for the observed difference:

(a) The alloy system investigated by Jamili et al. [37], contains a large fraction of RE in solid solution (WE43).
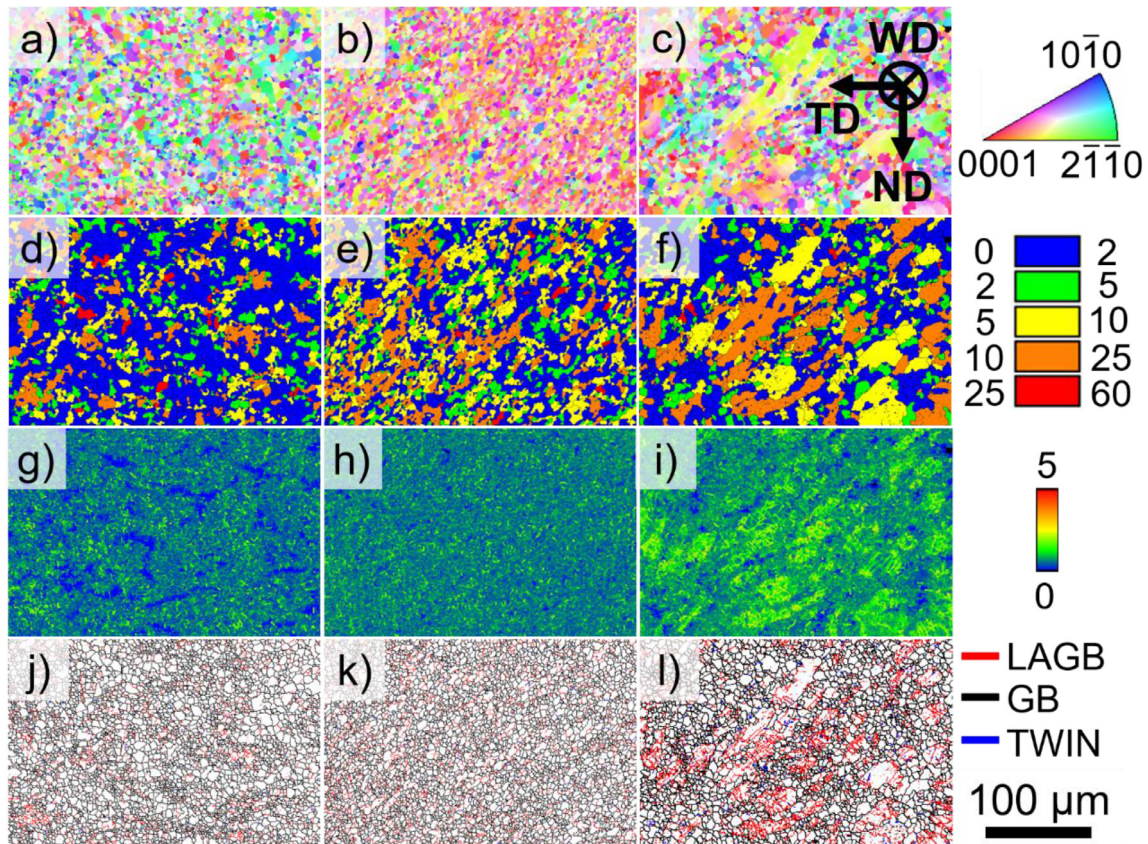
Fig. 6. Representative electron backscattered diffraction analysis of the joint of the ZK60–1.5RE alloy for the cross-section of the three distinct regions: (a,d,g,j) retrieving side of the thermomechanical affected zone; (b,e,h,k) stirred zone; (c,f,i,l) advancing side of the thermomechanical affected zone. a–c: inverse pole figure maps; D-f: grain orientation spread maps; (g–i) kernel average misorientation maps; (j–l) boundary maps.
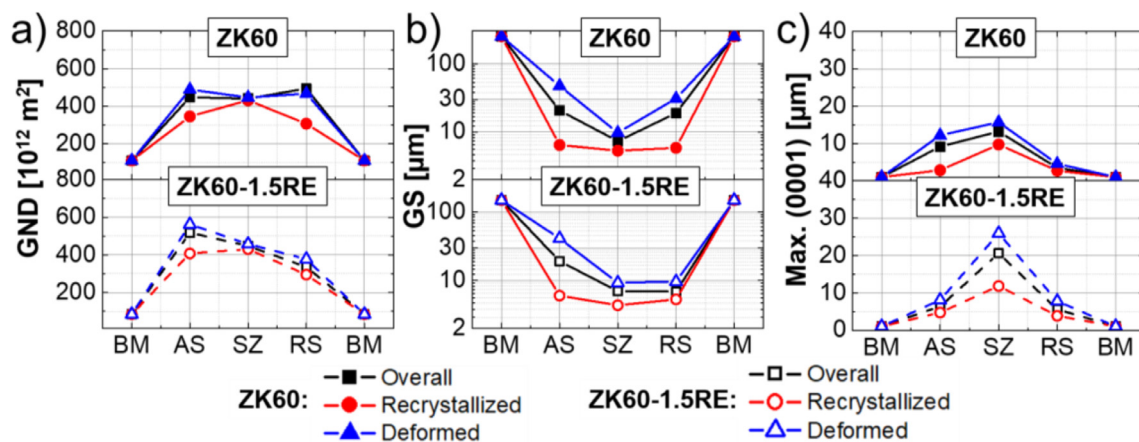

Fig. 7. Mean properties measured from the analysed electron backscattered diffraction measurements for the investigated cross-sections of the ZK60 and ZK60–1.5RE: (a) Overall, recrystallised and deformed geometric necessary dislocation (GND) density; (b) Overall, recrystallised and deformed grain size; (c) Overall, recrystallised and deformed maximum intensity of the pole figure for the (0001).

Gourdet and Montheillet [62] shown that the RE reduce the texture of deformed alloys by promoting the growth of grains in different directions during recrystallization, thus decreasing the anisotropy. The Ce is found mainly as intermetallic compounds in the ZK60–1.5RE [38]. Therefore it has a limited impact on reduced effect on the texture development during FSW

(b) The investigated material by Jamili et al. [37] and Gourdet and Montheillet [62] were wrought materials. Here, the material initially is in the as-cast material.

Therefore, the comparison with the BM will always show a higher texture value. The higher values of texture observed at the FSW of the ZK60–1.5RE than the ZK60 can probably be related to the higher stresses required to deform the ZK60–
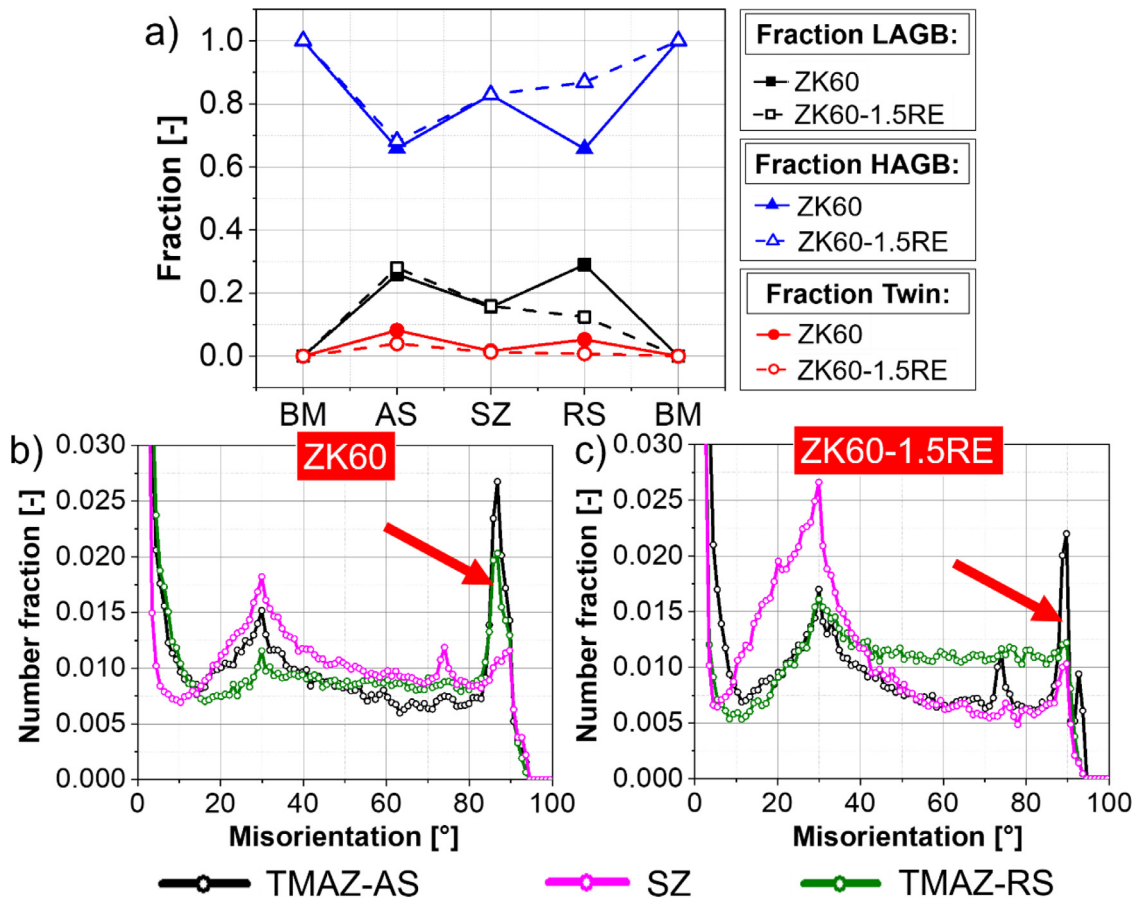
Fig. 8. (a) Average low angle grain boundary (LAGB), high angle grain boundary (HAGB) and tensile twin $\{10\bar{1}2\}\langle1\bar{2}10\rangle$, fractions for the base metal (BM), thermomechanical affected zone in the advancing side (AS), thermomechanical affected zone in the advancing side (RS), and the stirred zone (SZ) of the joints for the ZK60 and ZK60–1.5RE alloys; (b,c) Boundary misorientation angle distributions for the ZK60 and ZK60–1.5RE, respectively.

1.5RE (higher torque, Fig. 1). This crystallographic anisotropy should also impact the mechanical properties of the joints. Thus, different tensile, toughness and fatigue behaviours are expected for different joint orientations.

The average fraction of low angle grain boundary, tensile twins $\{10\bar{1}2\}\langle1\bar{2}10\rangle$, and high angle grain boundaries are shown in Fig. 8a for the different regions of the joint for the ZK60 and ZK60–1.5RE. Due to plastic deformation, low angle grain boundaries are formed at the TMAZ and tensile twins. The twin boundary fraction is more pronounced for the ZK60 than the ZK60–1.5RE, but its maximum value is still less than 10% for the highest fraction in the TMAZ in the AS. A partially recrystallised microstructure is observed in the SZ, and the volume fraction of high angle grain boundaries is ˜80%, and the fraction of twin boundaries is negligible in this region. The boundary misorientation angle distributions of the TMAZ at the AS, TMAZ at the RS, and the SZ are shown in Fig. 8(b and c) for the ZK60 and ZK60–1.5RE, respectively. The misorientation distribution is limited to a number fraction of 0.03, but the fraction of low angle grain boundaries with very low misorientation is larger than 0.03 in all measured conditions. A peak in boundary misorientation at ˜90° due to tensile twins $\{10\bar{1}2\}\langle1\bar{2}10\rangle$ is observed and indicated with the red arrow. This peak at ˜90° shows the highest number frac-

tion for the ZK60 and the TMAZ at the AS. A second peak is observed at ˜30° The strong basal texture that is developed during FSW for the investigated alloys can explain the limited increase in boundary misorientation angle up to ˜30° Thus, since the textural effect is the highest in the SZ of the ZK60–1.5RE (Fig. 7c), the peak at ˜30° is the highest for this condition. The value of the peak at 30° can be directly related to the maximum intensity of the pole figure for the (0001): the higher the value of the peak at 30° in Fig. 8(b,c), the higher the maximum intensity of the basal texture (Fig. 7c).

The anisotropy of the different regions of the joint for the ZK60 and ZK60–1.5RE are assessed by the inverse pole figures (IPF) shown in Fig. 9. Due to the complexity in determining the specific directions of the plastic deformation during FSW, the IPFs are shown so that the welding direction is perpendicular to the measured cross-section. A pole slightly rotated from the (0001) is observed in all cases, and the maximum value of crystallographic texture is observed at the SZ for the ZK60–1.5RE.

3.3. Mechanical properties

The hardness maps of the investigated joints are shown in Fig. 10 for the ZK 60 and ZK60–1.5RE. The average value
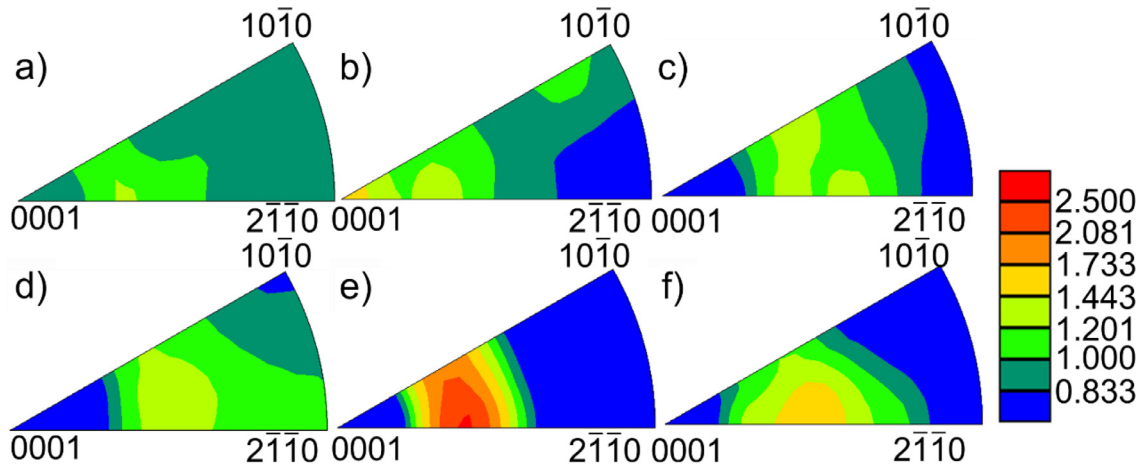
Fig. 9. Inverse pole figures for the different weld regions analysed in their cross-sections of the produced joints of the ZK60 (a–c) and ZK60–1.5RE (d–f): (a,d) thermomechanical affected zone for the retrieving side; (b,e) stirred zone; (c,f) thermomechanical affected zone for the advancing side.
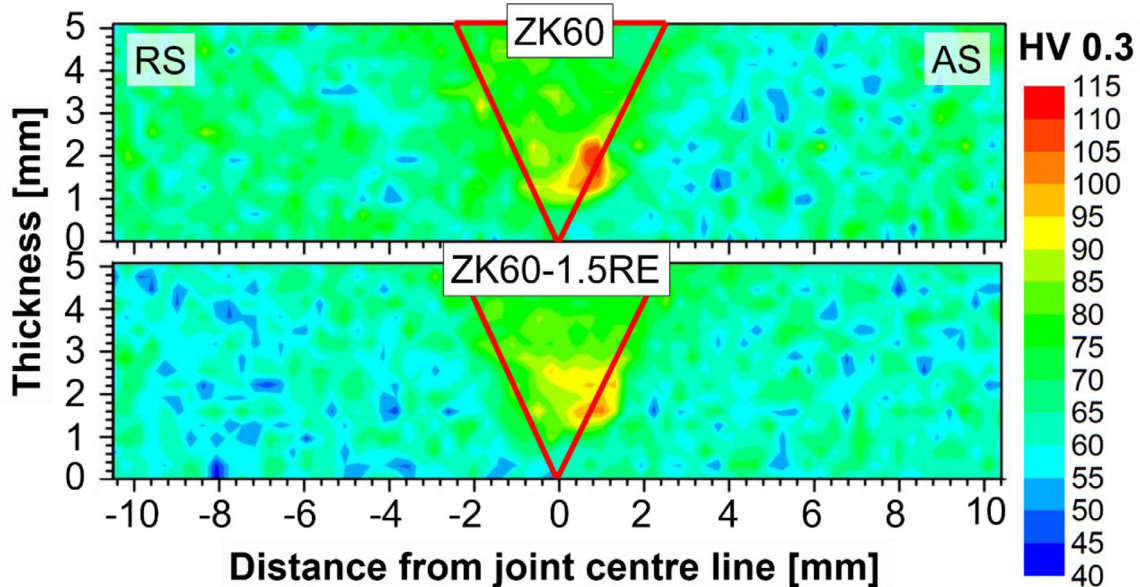

Fig. 10. Hardness maps of the cross-section measured for the ZK60 and ZK60–1.5RE joints. The red triangle indicates the position of the pin of the tool during welding.

of ˜75 HV is measured for both joints and is comparable to the base metal. A peak hardness of ˜115 HV and ˜100 HV is measured at the lower region of the stirred zone in the advancing side for the ZK60 and ZK60–1.5RE, respectively.

The room temperature mechanical properties were assessed using tensile testing, and the measured tensile tests are shown in Fig. 11a. The image analysis correlation maps to determine the local strain and the rupture location are shown in Fig. 11b. A slightly higher elongation is measured for the ZK60 compared to the ZK60–1.5RE. However, the ZK60 fractured at the joint, while the ZK60–1.5RE fractured at the BM. The localisation of strain in the AS in Fig. 11b is also related to the higher HV measured in the same region, as shown in Fig. 10. Asgari et al. [58] show that yield stresses of 153 MPa and 115 MPa, and elongations of 4.5% and 2% are achieved for the ZK60 and ZK60–1.5RE, respectively. They showed

that the mechanical strength and ductility are higher for the as-cast ZK60 alloy than the as-cast ZK60–1.5RE due to its increased solute content within the Mg-matrix and the smaller quantity of intermetallics that builds up an intermittent network. Therefore, the more inferior mechanical properties of the ZK60–1.5RE alloy compared to the ZK60 joint can be explained by the more inferior mechanical properties of the BM. FSW improves the mechanical properties of the as-cast microstructure of ZK60–1.5RE since it broke at the BM. The low strain localisation in the weld zone of the ZK60–1.5RE (Fig. 11c) shows the improvement of ductility and strength for the modified microstructure in the FSW joint.

The surface residual stress of both alloys measured using X-Ray diffraction is shown in Fig. 12. A peak of ˜70 MPa is measured at the TMAZ in the RS, while lower tensile stresses are measured in the TMAZ in the AS (˜10 MPa for
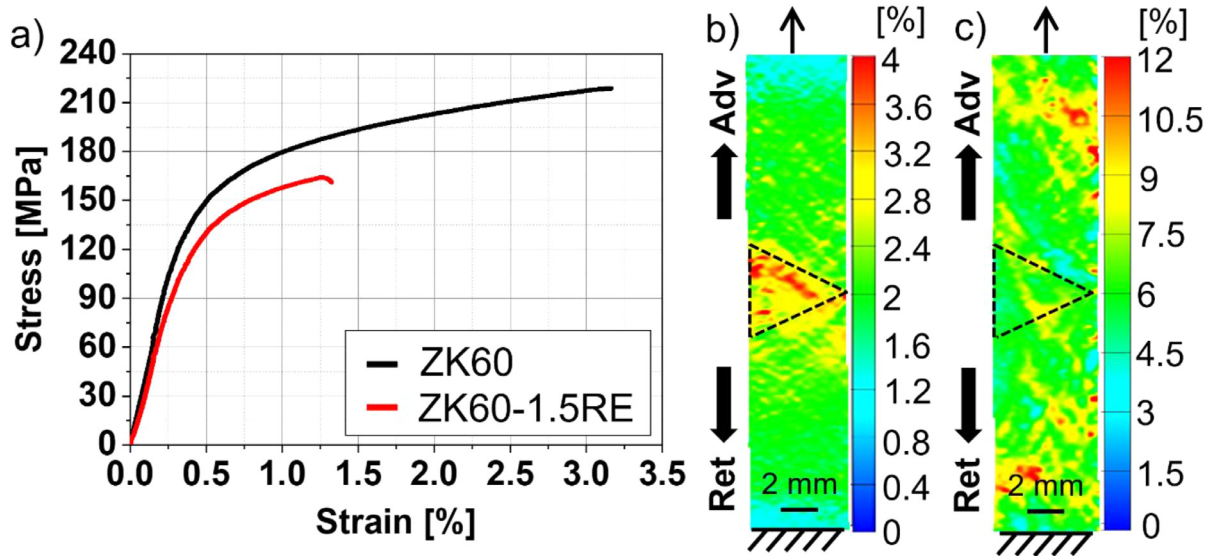
Fig. 11. Tensile testing for the produced joints tested at their cross sections: (a) measured engineering stress-strain curves; (b) image analysis correlation maps for the last acquisition before fracturing for the ZK60 joint; (c) image analysis correlation maps for the last acquisition before fracturing for the ZK60–1.5RE joint. The dashed black triangle indicates the position of the pin of the tool during welding.
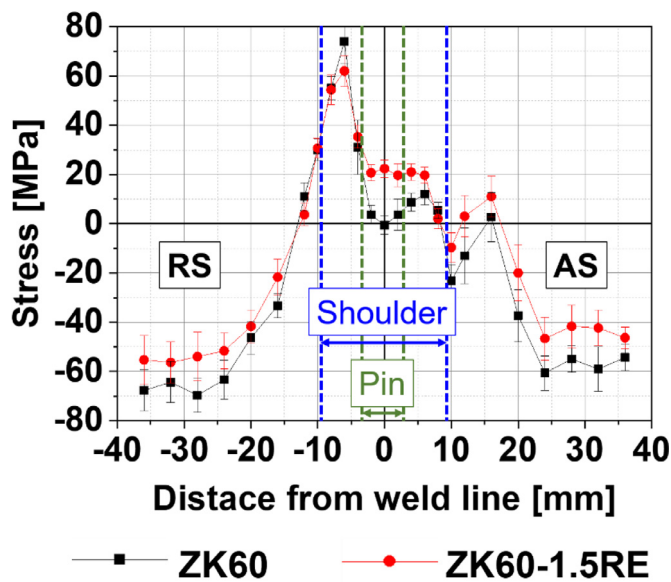

Fig. 12. Normal to surface measured residual stress measurements using X-ray diffraction of the similar joints of ZK60 and ZK60–1.5RE produced using linear friction stir welding.

the ZK60 and ˜20 MPa for the ZK60–1.5RE). The comparable behaviour of the surface residual stress between the ZK60 and the ZK60–1.5RE corroborates the similar microstructure formation observed in the different zone of the joints produced for the investigated alloys. The tensile stresses at the RS of the joints decrease the strength of the joints since lower applied stresses are needed to achieve the yield stress of the material. However, Fig. 11b shows that the fracture occurred at the AS of the ZK60 joint, where the surface residual stresses are not high. Therefore, the differences in microstructure and its effects on the tensile properties prevail over the surface residual stress effects for the produced joints.

4. Discussion

The complex mechanisms and material flow in typical linear FSW can result in a complex interaction between the material properties and the obtained joint. The RE addition in the ZK60 alloy and the possible restoration mechanisms that lead to the formation of the microstructure after FSW are correlated to the investigated microstructure and mechanical properties.

4.1. Influence of RE addition

The addition of 1.5RE to the ZK60 forms a semi-continuous network of intermetallic compounds along the grain boundaries [45]. On the other hand, dispersed particles of intermetallic compounds are observed at the grain boundaries for the ZK60 [45]. During plastic deformation, load partitioning occurs in multiphasic materials [46,47]. At room temperature, this effect is evidenced by the fracture of the tensile specimens at the BM for the ZK60–1.RE. The joint exhibited better properties than the BM for this alloy, while the opposite is observed for the ZK60 alloy. The dispersion and formation of fine intermetallic compounds as shown in Fig. 3 promote a more homogeneous deformation of the α-Mg matrix, avoiding the pile-up of dislocation intermetallic/α-Mg interfaces that can lead to local deformation and premature fracture. Despite the higher anisotropy of the SZ and TMAZ and higher dislocation density in those regions, the more homogenous deformation enhanced the ductility and the strength of the ZK60–1.5RE for the FSW joint.

At high temperatures, the microstructure evolution of all phases leads to a change in the load transfer [46]. The pressure of the welding tool normal to the surface can promote plastic deformation in regions where temperature increases. The extent of the plastic deformation rate is related to the

flow stress of the material for that temperature. In the case of the ZK60–1.5RE, a stronger network of intermetallic compounds in comparison to the flow stress of the α-Mg matrix leads to lower stress withstood by the α-Mg matrix for the same external applied load. Therefore, despite the lower value for the force normal to the surface applied for the FSW of the ZK60, the plastic deformation rates are still higher in the α-Mg promoting the formation of a larger TMAZ.

However, once the α-Mg matrix starts to deform plastically notably, the difference in the measured microstructure features between the ZK60 and the ZK60–1.5RE is minimal compared to the differences between the different regions in the same joint (*Figs. 4* –9). Once plastic deformation occurs in the TMAZ and the SZ, the high temperatures, high strain rates, and high achieved strains promote the fragmentation of the intermetallic compounds, as shown in *Fig. 3*. The comparable properties of the joints of ZK60 and ZK60–1.5RE produced by FSW are also shown in the hardness maps (Fig. 10), tensile tests (Fig. 11), and surface residual stress measurements (*Fig. 13*).

4.2. Microstructure formation due to FSW

The formed microstructure results from the complex interaction of the several phenomena that can occur during FSW. From a typical globular-like dendritic microstructure, the investigated Mg alloys evolve towards a partially recrystallised and fine globular microstructure at the SZ. among the dynamic phenomena, continuous [48], geometric [49], and discontinuous dynamic recrystallisation [50,51], as well as dynamic recovery [52], and twining [53,54] are the main restoration mechanisms described for hot deformation of metallic materials. Static recovery and static recrystallisation play an important role in the microstructure formation after the dynamic microstructure modification [55]. Fig. 13 shows the typical microstructure of the TMAZ of the ZK60 at the RS. A heterogeneous microstructure can be observed in Fig. 13a, where a deformed grain is observed on the left bottom side involved in a partially recrystallised microstructure. Fig. 13 shows a grain reference orientation deviation axis map and a notable spread of orientation in axis rotation within the parent grain is observed for the deformed regions. It indicates that the temperature is not sufficiently high in the observed area to promote a fast rearrangement of the dislocations into cells. Thus, deformed regions with large misorientation spread are formed, as highlighted in the misorientation profile in Fig. 13d by the dashed blue ellipses. Moreover, the presence of tensile twins $\{10\bar{1}2\}\langle1\bar{2}10\rangle$ is visible and highlighted in the misorientation profile in Fig. 13d. Furthermore, Fig. 13c shows the kernel average misorientation map for the investigated region, and the regions with large kernel values are more often observed along the grain boundaries. The reduced role of dynamic recovery in low stacking fault materials, and the lack of active slip systems in hcp systems [56–58], such as Mg, lead to the formation of a highly misoriented material where the dislocation, thus the strain, are accumulated along the grain boundaries.

Similarly to the RS, a deformed and heterogeneous microstructure is observed in Fig. 13e. Three misorientation profiles are shown in Fig. 13f. In the misorientation profile "MP1", three twins are observed with a thickness of ~3 μm. The large plastic deformation leads to the formation of a misorientation spread and low angle grain boundaries with the twinned regions in the analysed region, as highlighted in the inset in Fig. 13f and shown in the misorientation profile "MP2". The formation of low angle grain boundaries is shown in "MP3", evidencing that dynamic recovery and subgrain formation are also active phenomena for the microstructure modification at the TMAZ in the investigated Mg alloys. Despite the low stacking fault energy of Mg alloys, the increase in temperature can activate more slip systems, promoting gliding [59–61]. Thus, for favourable orientated grains, the plastic deformation can lead to the multiplication of dislocation and rearrangement in sharp subgrain boundaries.

The formation of a necklace of recrystallised grains along the grain boundaries is observed in Fig. 13a and more evident in Fig. 4, as indicated by the red circle. This is a typical microstructure obtained during static recrystallisation [55] or discontinuous dynamic recrystallisation [50,51]. In both cases, the larger the deformation, the higher the recrystallisation grade since the stored energy for recrystallisation increases with increased deformation [55]. Higher temperatures lead to higher nucleation and higher mobility of the high angle grain boundaries, accelerating especially the static recrystallisation. In discontinuous dynamic recrystallisation, the dependency is not straightforward since the increment In temperature can reduce the dislocation density, reducing nucleation, thus recrystallisation kinetics.

For any portion of the material in the TMAZ, there is a distribution of plastic deformation and temperatures. Thus, with the advance of the tool during FSW, the material deforms cold, and twins and misorientation spread within the grains are formed. With the increase in temperature, reorganisation of the dislocations, and sharp low-angle grain boundaries are formed. For regions with large deformation and large temperatures, static and discontinuous dynamic recrystallisation plays a role in forming a partial recrystallisation microstructure.

Therefore, the microstructure formation in the TMAZ can be summarised as follows:

- The colder regions in the TMAZ closer to the BM exhibit higher twinning activity, lower recrystallisation grade, and grains with large misorientation spread.
- Towards the SZ, the deformation increases as well as the temperature. Therefore, a progressive increase in sharp low angle grain boundary formation is observed.
- With an increase in peak temperature towards the SZ, the role of discontinuous or static recrystallisation increases, and the formation of a partially recrystallised microstructure is observed.

At the stirred zone, the peak temperature, strain, and strain rates achieved during FSW are higher than the TMAZ.
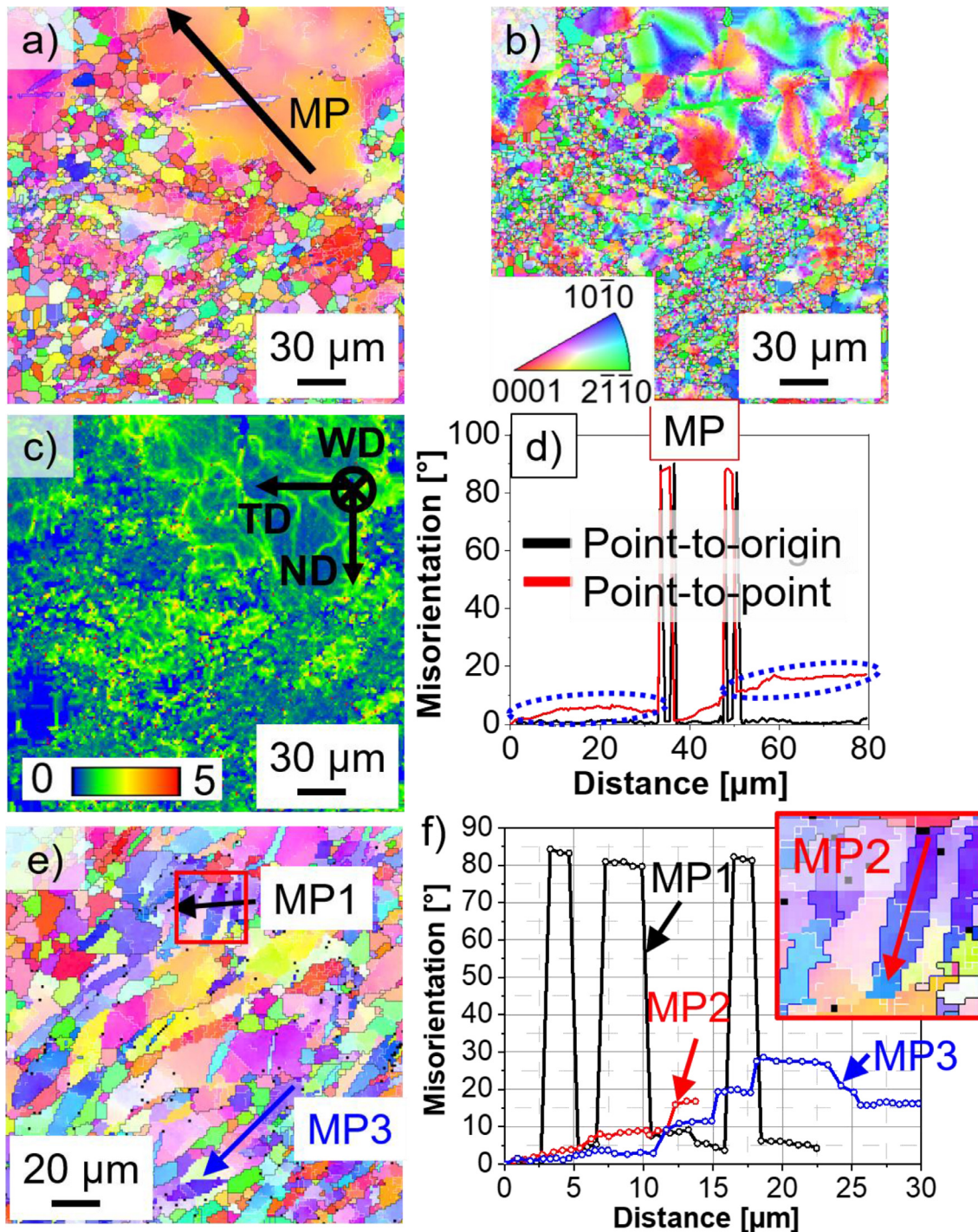
Fig. 13. Detailed regions of the thermomechanical affected zone of the ZK60 alloy in the: (a–d) RS; (e,f) AS. (a) Inverse pole figure map where the misorientation profile indicated by "MP" is shown in (d). (b,c) Grain reference orientation deviation axis map and kernel average misorientation map of the region shown in a), respectively. (e) inverse pole figure map where the misorientation profiles "MP1" and "MP3" are shown in (f). The highlighted region with the red square is shown as an inset in (f) where the misorientation profile"MP2" within a twin is shown. In the inverse pole figure maps, low angle grain boundaries with misorientation between 2° and 15° are marked in white, and tensile twins $\{10\bar{1}2\}\langle1\bar{2}10\rangle$ are marked in blue. Grain boundaries are marked in black. (For interpretation of the references to colour in this figure legend, the reader is referred to the web version of this article.)

Fig. 14 shows the typical microstructure of the SZ of the joint of ZK60–1.5RE. The partially recrystallised microstructure comprises a mosaic of equiaxed-like subgrains and fine recrystallised grains. The large strains and high peak temperatures achieved at the SZ in the FSW alloys form a network of low and high angle grain boundaries. This typical microstructure can be formed during continuous dynamic recrystallisation [48,62]. The refined recrystallised microstructure that is shown in blue in the grain orientation spread in Fig. 14b (misorientation spread lower than 0.5°) indicate that they can also
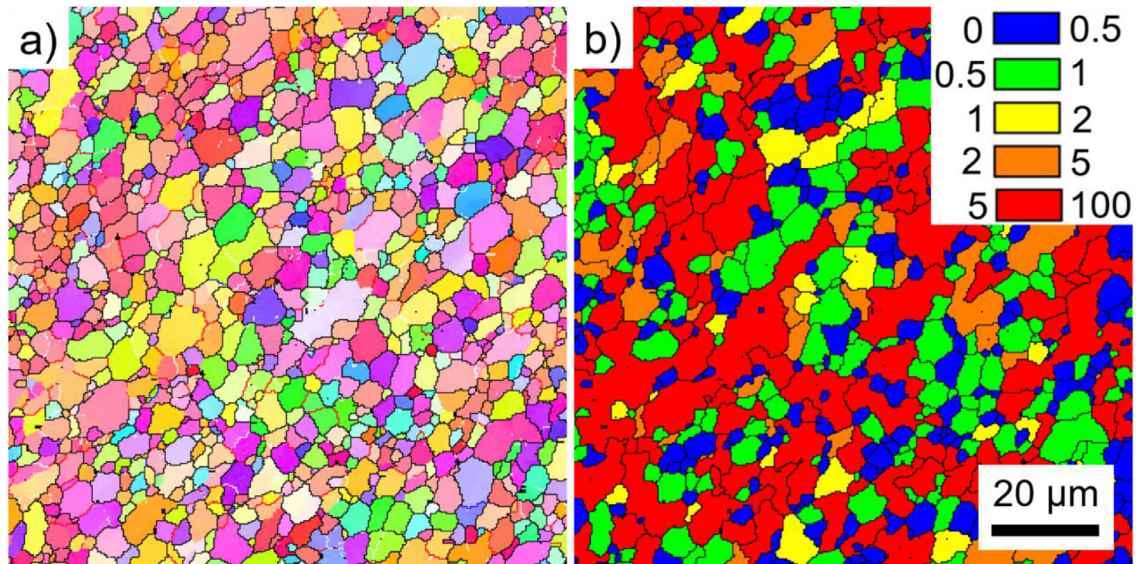
Fig. 14. Detailed region of the stirred zone of the ZK60–1.5RE: (a) inverse pole figure map; (b) grain orientation spread map. In (a), low angle grain boundaries with misorientation between 2° and 5°, and 5° to 15° are marked in white and red, respectively, and tensile twins $\{10\bar{1}2\}\langle1\bar{2}10\rangle$ are marked in blue. Grain boundaries are marked in black. (For interpretation of the references to colour in this figure legend, the reader is referred to the web version of this article.)

be formed either by discontinuous or continuous dynamic recrystallisation as well as static recrystallisation and it is not possible to distinguish which mechanism that was dominant or occurred.

The intermetallic compounds also play an important role are particle-stimulated nucleation (PSN) sites and can promote the formation of randomly oriented new grains [8,41,63,64]. The Mg_7Zn_3 and Zn_2Zr particles present in both alloys and the $MgZn_2Ce$ with high thermal stability present in the ZK60–1.5RE could also serve as PSN. Its role is expected to be higher in regions where is size is not smaller than 1 μm. Thus, it should have a minor role in the microstructure formation at the SZ. However, PSN can explain the formation of recrystallised grain in regions of the TMAZ, such as the ones highlighted by the red circle in Fig. 4d.

Therefore, several restoration mechanisms play a role in the deformation of the α-Mg matrix. The evolution of the activity of each mechanism is found as dependent on the deformation, temperature, and strain rate that is achieved in a specific region. Despite being named TMAZ and SZ, a sharp division in specific regions is not possible. A gradient microstructure from the BM towards the centerline of welding is observed.

5. Conclusions

Linear friction stir welding was used for similar welding of plates of as-cast ZK60 and ZK60–1.5RE alloys. The microstructure of the produced joints is systematically characterised using optical, and electron microscopy. The EBSD measurements are used to provide insights on the possible mechanisms of microstructure formation during FSW and obtain the average microstructural features for the investigated alloys and regions of the joint. The mechanical properties are assessed using hardness, tensile testing, and surface resid-

ual stress measurements. The following conclusions can be drawn:

- The FSW improved the ductility and strength of the as-cast ZK60–1.5RE alloy since the tensile samples fractured in the BM.
- The α-Mg matrix deforms comparably for the ZK60 and ZK60–1.RE in the TMAZ and SZ. The differences in mean microstructural features in minimum between both alloys compared to the mean microstructural features in different regions of the same joint.
- The TMAZ of the ZK60 is larger than the TMAZ of the ZK60–1.5RE. Strengthening caused by the semi-continuous network of intermetallic compounds at the base metal of the ZK60–1.5RE and dispersed intermetallic compounds along the grain boundary can explain this behaviour.
- Colder regions that withstood little plastic deformation during FSW exhibit grains with tensile twins $\{10\bar{1}2\}\langle1\bar{2}10\rangle$ and large misorientation spread.
- A microstructure gradient is observed in the TMAZ of both alloys, and a partially recrystallised microstructure is formed towards the SZ.
- A mosaic-like microstructure composed of low and high angle grain boundaries is present in the stirred zone. Intensive dynamic recovery leading to subgrain formation and a microstructure that assembles a typical continuous dynamic recrystallised microstructure is observed. However, fine grain decorating the grain boundaries indicates that discontinuous dynamic recrystallisation, static recrystallisation, and/or particle stimulated nucleation also play a role in the microstructure formation during FSW of the investigated alloys.

Declaration of Competing Interest

Acknowledgments

References

[1] Y.N. Wang, C.I. Chang, C.J. Lee, H.K. Lin, J.C. Huang, Scr. Mater. 55 (2006) 637–640, doi:10.1016/j.scriptamat.2006.06.005.

[2] M. Hakamada, T. Furuta, Y. Chino, Y. Chen, H. Kusuda, M. Mabuchi, Energy 32 (2007) 1352–1360, doi:10.1016/j.energy.2006.10.020.

[3] A. Couret, D. Caillard, Acta Met. 33 (1985) 1447–1454, doi:10.1016/0001-6160(85)90045-8.

[4] A. Galiyev, R. Kaibyshev, G. Gottstein, Acta Mater. 49 (2001) 1199–1207, doi:10.1016/S1359-6454(01)00020-9.

[5] J. Soyama, R. Floriano, D.R. Leiva, Y. Guo, A.M. Jorge Junior, E. Pereira da Silva, H.C. Pinto, C. Bolfarini, C.S. Kiminami, W.J. Botta, Int. J. Hydrog. Energy 41 (2016) 11284–11292, doi:10.1016/j.ijhydene.2016.05.031.

[6] J. Soyama, M.R. Martins Triques, D.R. Leiva, A.M. Jorge Junior, E. Pereira da Silva, H.C. Pinto, C. Bolfarini, C.S. Kiminami, W.J. Botta, Int. J. Hydrogen Energy. 41 (2016) 4177–4184, doi:10.1016/j.ijhydene.2016.01.036.

[7] Y. WU, H. YAN, S. ZHU, J. CHEN, A. LIU, X. LIU, Trans. Nonferrous Met. Soc. China. 24 (2014) 930–939, doi:10.1016/S1003-6326(14)63145-9.

[8] H. Yu, Y.M. Kim, B.S. You, H.S. Yu, S.H. Park, Mater. Sci. Eng. A 559 (2013) 798–807, doi:10.1016/j.msea.2012.09.026.

[9] E.P. Silva, R.H. Buzolin, F. Marques, F. Soldera, U. Alfaro, H.C. Pinto, J. Magnes. Alloy. (2020), doi:10.1016/j.jma.2020.09.018.

[10] E.P. Silva, D.R. Leiva, R. Floriano, V.B. Oliveira, H.C. Pinto, W.J. Botta, Int. J. Hydrog. Energy. 45 (2020) 5375–5383, doi:10.1016/j.ijhydene.2019.05.207.

[11] R. Nandan, T. DebRoy, H.K.D.H. Bhadeshia, Prog. Mater. Sci. 53 (2008) 980–1023, doi:10.1016/j.pmatsci.2008.05.001.

[12] W.Y. Li, T. Fu, L. Hütsch, J. Hilgert, F.F. Wang, J.F. dos Santos, N. Huber, Mater. Des. 64 (2014) 714–720, doi:10.1016/j.matdes.2014.07.023.

[13] E.P. Silva, L.F. Batista, B. Callegari, V. Ferrinho, R.H. Buzolin, R.S. Coelho, F. Warchomicka, G.C. Requena, A.J. Ramirez, H. Pinto, Adv. Mater. Res. (2014) 688–693, doi:10.4028/www.scientific.net/AMR.922.688.

[14] S. Malopheyev, S. Mironov, V. Kulitskiy, R. Kaibyshev, Mater. Sci. Eng. A 624 (2015) 132–139, doi:10.1016/j.msea.2014.11.079.

[15] D.-H. Choi, S.-K. Kim, S.-B. Jung, J. Alloy. Compd. 554 (2013) 162–168, doi:10.1016/j.jallcom.2012.11.143.

[16] H. Fujii, R. Ueji, Y. Morisada, H. Tanigawa, Scr. Mater. 70 (2014) 39–42, doi:10.1016/j.scriptamat.2013.09.012.

[17] E.P. Silva, D.R. Leiva, H.C. Pinto, R. Floriano, A.M. Neves, W.J. Botta, Int. J. Hydrog. Energy. 43 (2018) 11085–11091, doi:10.1016/j.ijhydene.2018.04.209.

[18] M. Bobby Kannan, W. Dietzel, R. Zettler, J. Mater. Sci. Mater. Med. 22 (2011) 2397–2401, doi:10.1007/s10856-011-4429-x.

[19] T. Chen, W. Xue, Y. Li, X. Liu, J. Du, Mater. Chem. Phys. 144 (2014) 462–469, doi:10.1016/j.matchemphys.2014.01.020.

[20] Q. Liu, Q. Ma, G. Chen, X. Cao, S. Zhang, J. Pan, G. Zhang, Q. Shi, Corros. Sci. 138 (2018) 284–296, doi:10.1016/j.corsci.2018.04.028.

[21] R.C. Zeng, J. Chen, W. Dietzel, R. Zettler, J.F. dos Santos, M. Lucia Nascimento, K.U. Kainer, Corros. Sci. 51 (2009) 1738–1746, doi:10.1016/j.corsci.2009.04.031.

[22] G.L. Song, R. Mishra, Z. Xu, Electrochem. Commun. 12 (2010) 1009–1012, doi:10.1016/j.elecom.2010.05.011.

[23] M. Govindaraju, U. Chakkingal, P.R. Kalvala, R.V. Vignesh, K. Balasubramanian, J. Mater. Eng. Perform. (2020), doi:10.1007/s11665-020-04848-0.

[24] S.H. Chowdhury, D.L. Chen, S.D. Bhole, X. Cao, P. Wanjara, Mater. Sci. Eng. A 556 (2012) 500–509, doi:10.1016/j.msea.2012.07.019.

[25] J.F.C. Moraes, R.I. Rodriguez, J.B. Jordon, X. Su, Int. J. Fatigue. 100 (2017) 1–11, doi:10.1016/j.ijfatigue.2017.02.018.

[26] J. Zhang, X. Chen, D. Xia, G. Huang, A. Tang, B. Jiang, F. Pan, Mater. Sci. Eng. A 778 (2020) 139088, doi:10.1016/j.msea.2020.139088.

[27] M. Zhou, Y. Morisada, H. Fujii, J. Magnes. Alloy. 8 (2020) 91–102, doi:10.1016/j.jma.2020.02.001.

[28] J. Zhang, K. Liu, G. Huang, X. Chen, D. Xia, B. Jiang, A. Tang, F. Pan, Mater. Sci. Eng. A 773 (2020) 138839, doi:10.1016/j.msea.2019.138839.

[29] D. Liu, R. Xin, L. Zhao, Y. Hu, J. Alloy. Compd. 693 (2017) 808–815, doi:10.1016/j.jallcom.2016.09.187.

[30] N. Xu, R. Feng, Q. Song, Y. Bao, J. Mater. Res. Technol. 8 (2019) 4448–4456, doi:10.1016/j.jmrt.2019.07.056.

[31] K. Singh, G. Singh, H. Singh, J. Magnes. Alloy. 6 (2018) 399–416, doi:10.1016/j.jma.2018.06.001.

[32] B. Smola, I. Stulíková, J. Pelcová, B.L. Mordike, J. Alloy. Compd. 378 (2004) 196–201, doi:10.1016/j.jallcom.2003.10.099.

[33] J.F. Nie, B.C. Muddle, Acta Mater. 48 (2000) 1691–1703, doi:10.1016/S1359-6454(00)00013-6.

[34] X. Gao, S.M. He, X.Q. Zeng, L.M. Peng, W.J. Ding, J.F. Nie, Mater. Sci. Eng. A 431 (2006) 322–327 10.1016/j.msea.2006.06.018.

[35] N. Stanford, D. Atwell, M.R. Barnett, Acta Mater. 58 (2010) 6773–6783, doi:10.1016/j.actamat.2010.09.003.

[36] H. Yu, Y. Hongge, C. Jihua, S. Bin, Z. Yi, S. Yanjin, M. Zhaojie, J. Alloy. Compd. 586 (2014) 757–765, doi:10.1016/j.jallcom.2013.10.005.

[37] A.M. Jamili, A. Zarei-Hanzaki, H.R. Abedi, M. Mosayebi, R. Kocich, L. Kunčická, Mater. Sci. Eng. A 775 (2020) 138837, doi:10.1016/j.msea.2019.138837.

[38] E.P. Silva, F. Marques, T.S. Nossa, U. Alfaro, H.C. Pinto, Mater. Sci. Eng. A 723 (2018) 306–313, doi:10.1016/j.msea.2018.02.024.

[39] E.P. Silva, L.F. Batista, B. Callegari, I. Feierabend, R.H. Buzolin, R.S. Coelho, F. Warchomicka, G.C. Requena, H. Pinto, Adv. Mater. Res. 922 (2014) 694–699, doi:10.4028/www.scientific.net/AMR.922.694.

[40] S. Groh, E.B. Marin, M.F. Horstemeyer, D.J. Bammann, Model. Simul. Mater. Sci. Eng. 17 (2009) 075009, doi:10.1088/0965-0393/17/7/075009.

[41] J. Zhang, B. Chen, C. Liu, Mater. Sci. Eng. A 612 (2014) 253–266, doi:10.1016/j.msea.2014.06.058.

[42] ASM Handbook Volume 2: Properties and Selection: Nonferrous Alloys and Special-Purpose Materials, ASM international, 1990.

[43] E. Sharghi, A. Farzadi, J. Alloy. Compd. 748 (2018) 953–960, doi:10.1016/j.jallcom.2018.03.145.

[44] R. Jain, S.K. Pal, S.B. Singh, J. Inst. Eng. Ser. C 98 (2017) 37–43, doi:10.1007/s40032-016-0304-3.

[45] A.H. Ammouri, G. Kridli, G. Ayoub, R.F. Hamade, J. Mater. Process. Technol. 222 (2015) 301–306, doi:10.1016/j.jmatprotec.2015.02.037.

[46] J. Luo, L. Li, M. Li, Trans. Nonferrous Met. Soc. China 26 (2016) 414–422, doi:10.1016/S1003-6326(16)64130-4.

[47] D. Canelo-Yubero, C. Poletti, F. Warchomicka, J. Daniels, G. Requena, J. Alloy. Compd. 764 (2018) 937–946, doi:10.1016/j.jallcom.2018.06.097.

[48] Z.C.C. Sun, H.L.L. Wu, J. Cao, Z.K.K. Yin, Int. J. Plast. 106 (2018) 73–87.

[49] W. Blum, Q. Zhu, R. Merkel, H.J. McQueen, Mater. Sci. Eng. A. (1996), doi:10.1016/0921-5093(95)09990-5.

[50] T. Takaki, C. Yoshimoto, A. Yamanaka, Y. Tomita, Int. J. Plast. 52 (2014) 105–116, doi:10.1016/j.ijplas.2013.09.001.

[51] H. Li, C. Wu, H. Yang, nt. J. Plast. 51 (2013) 271–291, doi:10.1016/j.ijplas.2013.05.001.

[52] F.J. Humphreys, M. Hatherly, F.J. Humphreys, M. Hatherly, Recryst. Relat. Annealing Phenom. (2004) 415–Vhttps://doi.org/, doi:10.1016/B978-008044164-1/50017-7.

[53] M.R. Barnett, in: C. Bettles, M.B.T.A. in W.M.A. Barnett (Eds.), Woodhead Publ. Ser. Met. Surf. Eng., Woodhead Publishing, 2012: pp. 105–143. 10.1533/9780857093844.1.105.

[54] M.R. Barnett, Mater. Sci. Eng. A 464 (2007) 1–7, doi:10.1016/j.msea.2006.12.037.

[55] F.J. Humphreys, M. Hatherly, F.J. Humphreys, M. Hatherly, Recryst. Relat. Annealing Phenom. (2004) 215–IVhttps://doi.org/, doi:10.1016/B978-008044164-1/50011-6.

[56] J. Koike, T. Kobayashi, T. Mukai, H. Watanabe, M. Suzuki, K. Maruyama, K. Higashi, Acta Mater. 51 (2003) 2055–2065, doi:10.1016/S1359-6454(03)00005-3.

[57] M.M. Myshlyaev, H.J. McQueen, A. Mwembela, E. Konopleva, Mater. Sci. Eng. A 337 (2002) 121–133, doi:10.1016/S0921-5093(02)00007-2.

[58] S. Asgari, E. El-Danaf, S.R. Kalidindi, R.D. Doherty, Metall. Mater. Trans. A 28 (1997) 1781–1795, doi:10.1007/s11661-997-0109-3.

[59] T. Mayama, M. Noda, R. Chiba, M. Kuroda, Int. J. Plast. 27 (2011) 1916–1935, doi:10.1016/j.ijplas.2011.02.007.

[60] J.A. Yasi, L.G. Hector, D.R. Trinkle, Acta Mater. 59 (2011) 5652–5660, doi:10.1016/j.actamat.2011.05.040.

[61] F. Kang, Z. Li, J.T. Wang, P. Cheng, H.Y. Wu, J. Mater. Sci. 47 (2012) 7854–7859, doi:10.1007/s10853-012-6344-z.

[62] S. Gourdet, F. Montheillet, Acta Mater. 51 (2003) 2685–2699, doi:10.1016/S1359-6454(03)00078-8.

[63] S.W. Xu, K. Oh-ishi, S. Kamado, T. Homma, Scr. Mater. 65 (2011) 875–878, doi:10.1016/j.scriptamat.2011.07.053.

[64] S. Wang, R. Ma, L. Yang, Y. Wang, Y. Wang, J. Mater. Sci. 46 (2011) 3060–3065, doi:10.1007/s10853-010-5184-y.